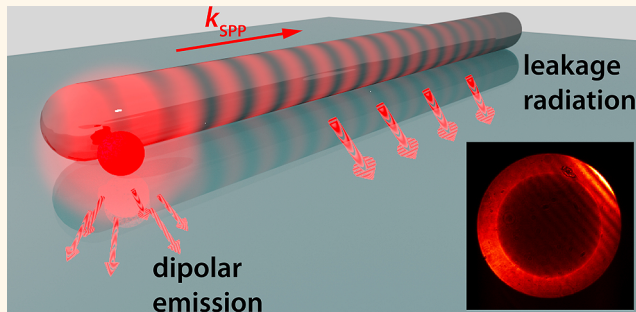


Radiation Channels Close to a Plasmonic Nanowire Visualized by Back Focal Plane Imaging

Nicolai Hartmann,[†] Dawid Piatkowski,^{†,‡} Richard Ciesielski,[†] Sebastian Mackowski,[‡] and Achim Hartschuh^{†,*}

[†]Department Chemie and CeNS, Ludwig-Maximilians-Universität München, 81377 München, Germany and [‡]Institute of Physics, Faculty of Physics, Astronomy and Informatics, Nicolaus Copernicus University, Grudziądzka 5, 87-100 Toruń, Poland

ABSTRACT We investigated the angular radiation patterns, a key characteristic of an emitting system, from individual silver nanowires decorated with rare earth ion-doped nanocrystals. Back focal plane radiation patterns of the nanocrystal photoluminescence after local two-photon excitation can be described by two emission channels: excitation of propagating surface plasmons in the nanowire followed by leakage radiation and direct dipolar emission observed also in the absence of the nanowire. Theoretical modeling reproduces the observed radiation patterns which strongly depend on the position of excitation along the nanowire. Our analysis allows us to estimate the branching ratio into both emission channels and to determine the diameter-dependent surface plasmon quasi-momentum, important parameters of emitter-plasmon structures.



KEYWORDS: plasmonics · metallic nanowires · rare earth ions · back focal plane imaging · upconversion

Propagating surface plasmon polaritons (SPPs) are electromagnetic waves bound to a metal–dielectric interface. They offer the distinguished possibility to concentrate light to subwavelength scales and transport this energy over a length several magnitudes larger.^{1–4} These properties provide the basis for plasmonics, a very active research area aiming at optical device miniaturization and the integration of optics and electronics on a single chip.^{5,6} Metallic nanowires (NWs) have drawn particular attention as plasmonic building blocks due to their successful implementation as waveguides,^{7–9} routers, and logic gates.^{10–12} SPPs on metallic NWs have been investigated by direct visualization,¹³ using a scanning aperture probe,¹⁴ by electrical detection¹⁵ as well as by calculations.¹⁶ A key step in plasmonic applications of NWs is the coupling of the initial energy source to the NW and the contributing energy relaxation pathways.^{17,18} Importantly, subwavelength light confinement by the SPPs can be used to enhance the interaction between objects and light.¹⁹ This coupling and the excitation

and propagation of SPPs have been experimentally visualized by leakage radiation microscopy^{20–22} combined with imaging of the back focal plane (BFP) for a variety of plasmonic structures and devices.^{23–25}

In this article, we studied the coupling of the emission from rare-earth-doped nanocrystals to SPP modes in silver NWs on glass. We use the ability of these nanocrystals to exhibit stable, nonbleaching upconverted photoluminescence (PL) on the anti-Stokes side of the laser energy²⁶ to avoid temporal intensity fluctuations and to exclude any background contribution from laser scattering, metal luminescence, or the sample substrate. Importantly, since two-photon excitation requires high excitation densities, it will only be efficient at the position of the laser focus. Two-photon excitation of NCs located outside of the focus along the NW mediated by propagating surface plasmons can be neglected due to limited light–plasmon coupling and plasmon damping. In addition, due to the extremely small oscillator strength of the nanocrystals at the emission wavelength reflected in a radiative

* Address correspondence to achim.hartschuh@cup.uni-muenchen.de.

Received for review September 3, 2013 and accepted October 11, 2013.

Published online October 12, 2013
10.1021/nn404611q

© 2013 American Chemical Society

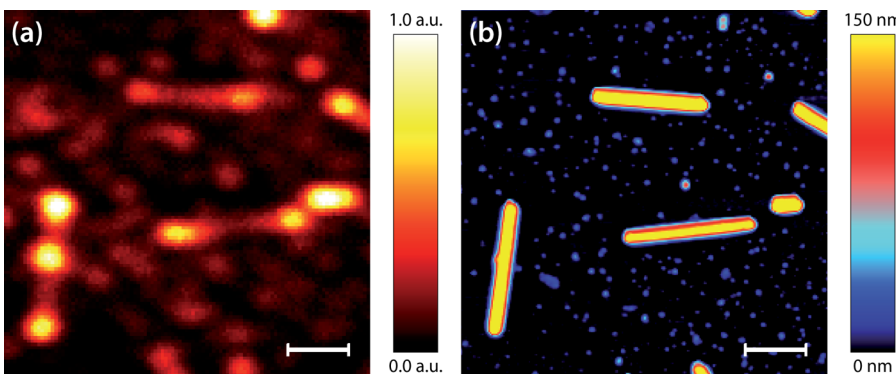


Figure 1. (a) Confocal PL map of a representative sample area together with the corresponding topography data in (b). In the PL map, the NWs show up as elongated structures with higher intensity at the NW ends. Several single PL spots are located around the NWs which can be attributed to single or small clusters of rare earth nanocrystals which can also be seen in the AFM data. The scale bar represents $2.0\text{ }\mu\text{m}$ in both images.

lifetime of the $f-f$ transitions in the microsecond regime,²⁶ plasmon-mediated coupling between nanocrystals located along the same NW can be neglected.⁹ With the help of the quantitative analysis of the recorded BFP patterns, we were able to separate the contributions of two different radiation channels, namely, the direct dipolar emission of the nanocrystals into the glass substrate, observed also in the absence of the NW, and the excitation of propagating SPPs in the NW. In addition to the branching ratio into these two channels, we obtained the SPP quasi-momentum, important parameters of active emitter-plasmon structures.^{17,27}

RESULTS AND DISCUSSION

First, a sample area of $100\text{ }\mu\text{m}^2$ was characterized by detecting the upconverted PL after excitation at 980 nm with a narrow band-pass filter centered at 670 nm with a full width at half-maximum of 10 nm in front of the avalanche photodiode used for signal detection (see Supporting Information, Figure 1). A representative PL image of a magnified sample area can be seen in Figure 1a. Subsequently, the same sample area was mapped *via* atomic force microscopy to measure the topographic height of each investigated NW. In the PL map (Figure 1a), the NWs appear as luminescent elongated structures with additional bright end spots or bright spots along the wire. In addition, weaker luminescent spots are distributed all over the sample. The topography of the same sample area (Figure 1b) shows the NWs at the same positions with lengths of several micrometers and heights between 100 and 250 nm as well as a number of smaller structures nearby (about 20 nm in height). The size of the smaller structures together with their luminescent behavior identifies them as single nanocrystals or small clusters of several crystals. From the PL signal (Figure 1a), it is evident that nanocrystals deposited in the vicinity of the NWs show enhanced PL and that the plasmonic enhancement is most efficient at the NW ends. Emission enhancement can result from

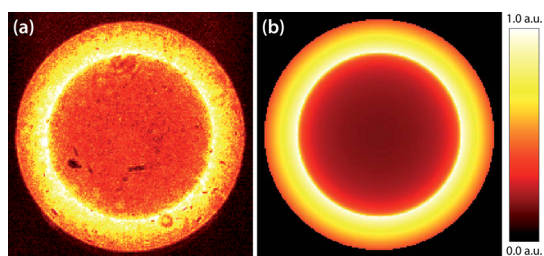


Figure 2. (a) Back focal plane PL emission pattern detected for a nanocrystal on glass. The detected angular range is limited by the maximum collection angle of the microscope objective that is given by its $NA = 1.4$. (b) Theoretical emission pattern for an isotropic emitter represented by two orthogonal in-plane and one out-of-plane point dipoles on glass. Calculated according to eq 1.

new radiation channels provided by the metal nanostructure corresponding to an increased local density of states.²⁸ In general, radiation channels are connected to characteristic angular distributions of emission that can be studied by BFP imaging^{29–31} (see Supporting Information, Figure 1).

To illustrate the change of the emission characteristics induced by the NW, BFP patterns of NCs without NWs were measured, filtering the detected signal for the upconverted PL (band-pass 670 nm). Figure 2a shows a representative example. The patterns consist of a radially symmetric intensity distribution that increases from the largest detectable angle given by the NA of the microscope objective toward the critical angle. For smaller angles, the pattern shows a more uniform and weaker intensity.

In the next step, BFP patterns were recorded for different NWs at varying excitation positions along the NW, again filtering the detected signal for the upconverted PL. Figure 3a shows a representative example of the PL map of a single NW together with the excitation positions and the recorded BFP patterns (Figure 3b–d). Other examples for nanowires of different diameters are shown in the Supporting Information, Figure 2. When the NW is excited in the middle, the BFP image

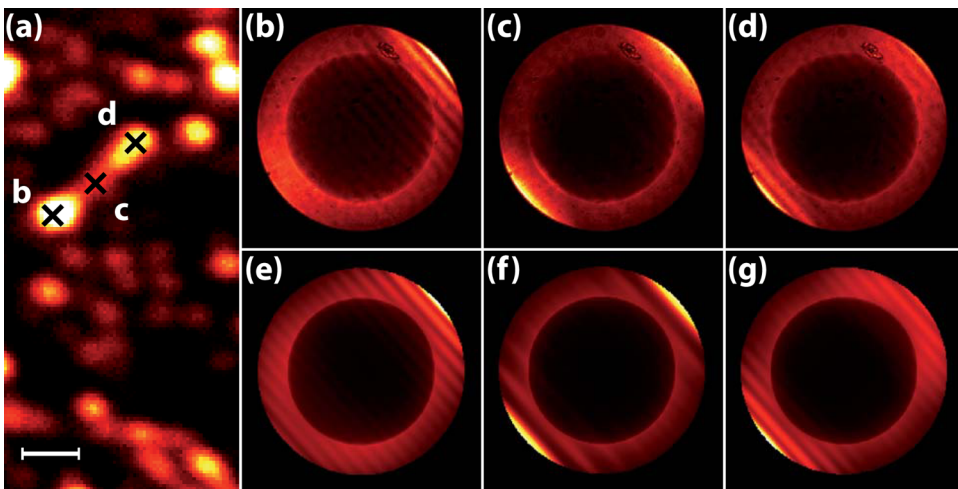


Figure 3. (a) Confocal PL map of a wire decorated with nanocrystals. The scale bar represents $2.0 \mu\text{m}$. Upon excitation at different positions (b–d), the corresponding BFP patterns (b–d) were recorded. The detected angular range is limited by the maximum collection angle of the microscope objective that is given by its $\text{NA} = 1.4$. The lower row (e–g) shows the corresponding theoretical patterns obtained from a superposition of plasmon leakage radiation from the NW and direct dipolar emission calculated according to eq 4. Each BFP pattern is scaled to its maximum intensity, respectively.

(Figure 3c) shows a symmetric pattern oriented along the NW axis with two brighter lobes at the rims of the pattern. In contrast, the patterns recorded upon excitation of the NW ends (Figure 3b,d) exhibit an asymmetric intensity distribution with the lobes on the opposite side of the excitation position being brighter than the other. In addition, a fringe pattern is visible when the NW is excited at the ends. This indicates that the position of excitation strongly influences the angular emission characteristics of the NW.

In order to analyze the measured BFP patterns and to extract the contributing radiation channels, we start from the two apparent signal contributions.

The first signal contribution stems from nanocrystal emission which is not coupled to the NW as presented for nanocrystals in the absence of a NW (Figure 2a). A single nanocrystal contains between 10^2 and 10^4 dipolar emission centers without preferred orientation, thus the resulting BFP pattern can be treated as the sum of patterns from randomly oriented dipoles. This contribution is modeled using the theoretical description of dipolar emission on an interface from Lieb *et al.*²⁹ Due to the symmetry of the resulting functions, the random orientation of dipoles can be represented by two orthogonal in-plane dipoles and an additional dipole perpendicular to the surface, also indicated in Figure 4a by black arrows. Thus the intensity in the BFP can be described by the sum of the individual patterns of the single dipoles:

$$I_{\text{NC}}(\vec{k}_{\text{BFP}}) = I_{\text{dipole},x} + I_{\text{dipole},y} + I_{\text{dipole},z} \quad (1)$$

as depicted in Figure 2b and Figure 4a.

The second contribution originates from SPPs launched by nearby nanocrystals propagating along the NW surface which are detected as leakage radiation.^{20,22} A characteristic signature of this radiation channel is

the fringe pattern in the BFP image that results from the finite length of the NW in the micrometer range emitting *via* leakage radiation. We describe this channel by a leaky 1D antenna resonator model, following Taminiau *et al.*³² The configuration is defined by the finite NW length L , the wire orientation given by the in-plane angle Ψ , and the input excitation at the position a (Figure 4b). Plasmon propagation depends on k_{SPP} supported by the NW and a complex reflection coefficient at its end including the phase change ϕ taken up with each reflection:

$$r = |r| \cdot e^{i\phi}; \quad 0 \leq |r| \leq 1 \quad (2)$$

In order to include losses in the metal, the plasmon wavevector k_{SPP} is defined as a complex value in direct correlation with the propagation length L_D .¹

$$k_{\text{SPP}} = k_{\text{SPP}}' + ik_{\text{SPP}}'' = k_{\text{SPP}}' + i \frac{1}{2L_D} \quad (3)$$

Here we also consider the air/glass interface on which the NW is deposited by multiplying the antenna BFP intensity distribution taken from ref 32 with the BFP pattern of an in-plane dipole-oriented parallel to the wire axis I_{dipole}^{Ψ} :

$$I_{\text{NW}}(\vec{k}_{\text{BFP}}) = I_{\text{dipole}}^{\Psi} \times \left| \frac{i}{1 - r^2 e^{2ik_{\text{SPP}}L}} \left(A \left[\frac{re^{ik_{\text{SPP}}L} e^{-i(k_{\parallel} - k_{\text{SPP}})z}}{k_{\parallel} - k_{\text{SPP}}} - \frac{e^{-i(k_{\parallel} + k_{\text{SPP}})z}}{k_{\parallel} + k_{\text{SPP}}} \right]_a^{a-L/2} \right. \right. \\ \left. \left. + B \left[\frac{e^{-i(k_{\parallel} - k_{\text{SPP}})z}}{k_{\parallel} - k_{\text{SPP}}} - \frac{re^{ik_{\text{SPP}}L} e^{-i(k_{\parallel} + k_{\text{SPP}})z}}{k_{\parallel} + k_{\text{SPP}}} \right]_a^{L/2} \right) \right|^2 \quad (4) \right.$$

with

$$A = e^{ik_{\text{SPP}}a} + re^{ik_{\text{SPP}}L} e^{-ik_{\text{SPP}}a} \\ B = re^{ik_{\text{SPP}}L} e^{ik_{\text{SPP}}a} + e^{-ik_{\text{SPP}}a} \quad (5)$$

and

$$\begin{aligned} \vec{k}_{\parallel} &= \vec{k}_{\text{BFP}} \cdot \vec{e}_{\text{NW}} \\ \vec{e}_{\text{NW}} &= \begin{pmatrix} \cos(\Psi) \\ \sin(\Psi) \end{pmatrix} \end{aligned} \quad (6)$$

Figure 4b shows a representative NW BFP pattern I_{NW} calculated for a wire with a length of $L = 4.0 \mu\text{m}$, a diameter of 200 nm, and a plasmon wavevector of $k'_{\text{SPP}} = 1.648 \times 10^7 \text{ m}^{-1}$ predicted for SPPs in nanowires surrounded by glass excited at the nanocrystal emission at 670 nm.^{24,33} The modulus of the reflection coefficient $|r|$ was taken to be 0.3, the phase shift $\phi = 100^\circ$,³⁴ and the excitation position $a = 200 \text{ nm}$ away from the wire end. Together with the clearly visible fringes resulting from the finite wire length, the schematic in Figure 4b illustrates the formation of the BFP pattern which explains the asymmetry in the intensity distribution that is also seen in the experimental patterns after exciting the wire at the ends (Figure 3b,d). If the NW is excited at the left end, SPPs can travel only to the right. In Fourier space, the wavevector components are sorted by their propagation direction. Therefore, it is evident that the excitation in the middle of the NW results in a symmetric BFP pattern with similar intensities on both sides (Figure 3c,f). The influence of the excitation of the excitation position a on the BFP pattern is shown in detail in the Supporting Information, Figure 3. The present model treats the several micrometers long NWs as quasi-1D structures. For shorter NWs with considerably smaller aspect ratio, the contribution of sub- and super-radiant modes becomes more significant.^{32,35,36}

We fitted all experimental BFP patterns with a combination of the NW pattern I_{NW} and the pattern consisting of randomly oriented dipoles I_{NC} :

$$I_{\text{BFP,fit}}(D, W, k'_{\text{SPP}}, L, L_{\text{D}}, a) = D \cdot I_{\text{NC}} + W \cdot I_{\text{NW}}(k'_{\text{SPP}}, L, L_{\text{D}}, a) \quad (7)$$

After adjusting the orientation angle Ψ with respect to the NW axis, the free fit parameters were the amplitudes of the different channel contributions D and W , the real part of the plasmon wavevector k'_{SPP} together with the propagation length L_{D} , the wire length L , and the NC position a . Representative fits of experimental BFP patterns are shown in Figure 3e,f and in the Supporting Information, Figure 2. The fitted patterns agree very well with the experimental results supporting our simplified model describing the emission by the two distinct channels. Moreover, the optically derived NW length L that is the source of the characteristic fringe patterns is in general agreement with the values determined by AFM (see Supporting Information, Figure 4).

Besides the two emission channels used in our model, forward scattering at the nanowire end leading to a radiation cone as reported by Li *et al.*³⁷ could occur. From the good agreement between the experimental

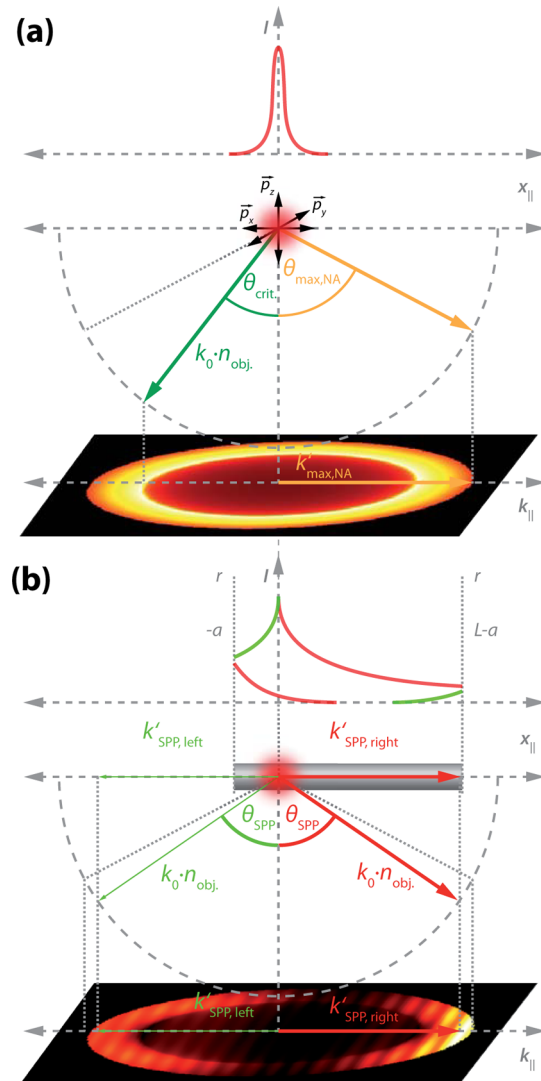


Figure 4. (a) BFP pattern for randomly oriented dipoles represented by two orthogonal in-plane and one out-of-plane dipole, indicated by black arrows. Also indicated are the projections of the critical angle, θ_{crit} , the maximum detectable angle, $\theta_{\text{max,NA}}$, and k vector, $k_{\text{max,NA}}$, determined by the objective NA. (b) Resulting BFP pattern for the leaky antenna resonator as described in eq 4. Indicated by the arrows are the wavevectors for the right (red $k'_{\text{SPP},\text{right}}$) and the left (green $k'_{\text{SPP},\text{left}}$) direction and their projection onto the Fourier plane after leaking into the glass substrate at the resonance angle θ_{SPP} given by $k'_{\text{SPP}} = k_0 n_{\text{obj}} \sin \theta_{\text{SPP}}$.

data and the fitting results, we conclude that the relative contribution of such an additional channel cannot be substantial in the present system.

Since the theoretical BFP patterns used in the fit for the NC and the NW were normalized to the intensity radiated into all possible angles below and above the air/dielectric interface

$$\int_0^\pi \int_0^{2\pi} I_{\text{NC}} d\varphi d\theta = 1, \int_0^\pi \int_0^{2\pi} I_{\text{NW}} d\varphi d\theta = 1 \quad (8)$$

the amplitudes D and W can be seen as the number of photons emitted *via* each channel. The branching ratio F between the two radiation channels, which reflects

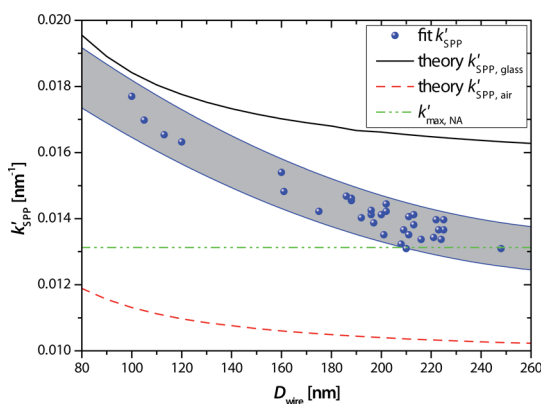


Figure 5. Fitted k'_SPP is plotted against the thickness for each corresponding wire together with the uncertainty of the fit indicated by the gray shaded area. The black solid and the red dashed lines represent the theoretical k' values for the SPP at the metal–glass interface $k'_{SPP,glass}$ and at the metal–air interface $k'_{SPP,air}$, based on ref 33. Indicated by the green dashed dotted line is the maximum detectable $k'_{max,NA}$ with the used microscope objective (NA = 1.4).

the coupling strength between NC and NW, can be defined as $F = W/D$. For the 49 studied NW positions, this branching ratio was found to be 0.7 ± 0.3 on average. No correlation between NW diameter and branching ratio was observed. The spread in F probably reflects different NC to NW distances also caused by different thicknesses of the polymer layer covering the nanowires.

We note the finite length L of the NW over which it emits *via* leakage radiation leads to a fringe pattern in the BFP enabling the determination of k'_SPP even if k'_SPP lies outside the detectable wavevector range of the microscope objective (Figure 5). In order to compare the values for k'_SPP determined by fitting the BFP patterns for the different NWs with theoretical calculations, we used the model of thin metal cylindrical waveguides.³³ This model was already employed for similar silver NWs to calculate k'_SPP for a given wire thickness.²⁴ As shown in Figure 5b for larger NW

diameters, the experimental values k'_SPP are situated between the theoretical k' values for the SPPs at the metal–glass and metal–air interfaces. This is a strong indication for a hybridized plasmon as described by Shegai *et al.*²⁴ For decreasing wire thickness, the values approach the larger and more bound $k'_{SPP,glass}$. While the fitting results for the propagation length L_D do not show a clear correlation with the nanowire diameter, most likely due to varying surface scattering losses and reflectivities r , we observe a weak trend of increasing L_D for larger diameters. This trend agrees with recent theoretical predictions by Li and Qiu³⁸ indicating that longer propagation lengths in thicker nanowires result from reduced ohmic losses due to a decreasing fraction of energy within the silver.

CONCLUSIONS

By recording the radiation patterns of a coupled system of rare earth nanocrystals and silver nanowires in the back focal plane, we found that the emission in the vicinity of a nanowire can be approximately described by two emission channels that can be calculated analytically: dipolar emission, also observed in the absence of the nanowire, and leakage radiation from the nanowire. The latter can be calculated using an antenna resonator model that considers the air–dielectric interface on which the nanowire is deposited and the position of excitation along the nanowire. Fitting of the experimentally observed patterns provides estimates of the ratio F of photons emitted *via* the nanowire mediated and dipolar channels with mean value of $F = 0.7$. Finally, the fit of the back focal plane patterns gives access to the wavevector k'_SPP of the SPP supported by the nanowire. Our results are important for plasmonic applications of nanowires since the understanding of emission characteristics, coupling efficiency, and SPP properties supported by such nanowires plays a key role in device integration.

METHODS

Experimental Setup. A conventional inverted confocal microscope with an oil immersion objective (NA = 1.4) and a laser source operating at 980 nm was used. Detection of scanning confocal signals and back focal plane (BFP) patterns followed the setup described in ref 31. A detailed description is given in the Supporting Information.

Subsequently, the same sample area was mapped *via* atomic force microscopy (AFM) (Nanoink DPN System, tapping mode, constant amplitude) to measure the topographic height of each investigated nanowire.

Materials. The used sample consisted of silver nanowires with diameters between 100 and 250 nm and lengths up to several micrometers,³⁹ spin-coated on a microscope glass coverslide. In a second step, erbium- and ytterbium-doped $NaYF_4$ nanocrystals⁴⁰ were spin-coated on top of the nanowire sample. On the basis of a dopant concentration of 2 wt % Er and the cubic lattice structure of $NaYF_4$, we can estimate the number of emitting centers for a NC with a diameter of 20 (50) nm to be ≈ 600 (9200).

Conflict of Interest: The authors declare no competing financial interest.

Acknowledgment: The authors thank Maria Olejnik (Nicolaus Copernicus University, Torun, Poland) for the supply of silver nanowire samples, Marcin Nyk (Wroclaw University of Technology, Wroclaw, Poland) for the rare earth nanocrystal samples, and Angela Wochnik (LMU) for TEM measurements. This work was financially supported by the DFG through the Nanosystems Initiative Munich (NIM), the ERC (starting Grant NEWNANOSPEC), and the Polish National Science Centre (Project N N202 238940), and Mobility Plus (project 633/MOB/2011/0) founded by the Polish Ministry of Science and Higher Education.

Supporting Information Available: Detailed information on the optical setup (Supporting Information, Figure 1). Back focal plane images for nanowires with different diameter (Supporting Information, Figure 2). Influence of the excitation position on the back focal plane pattern (Supporting Information, Figure 3). Determination of the nanowire length from fits of the BFP pattern and from AFM measurements (Supporting Information,

Figure 4). This material is available free of charge via the Internet at <http://pubs.acs.org>.

REFERENCES AND NOTES

- Raether, H. *Surface Plasmons on Smooth and Rough Surfaces and on Gratings*; Springer: Berlin, 1986.
- Gramotnev, D. K.; Bozhevolnyi, S. I. Plasmonics beyond the Diffraction Limit. *Nat. Photonics* **2010**, *4*, 83–91.
- Ozbay, E. Plasmonics: Merging Photonics and Electronics at Nanoscale Dimensions. *Science* **2006**, *311*, 189–193.
- Han, Z.; Bozhevolnyi, S. I. Radiation Guiding with Surface Plasmon Polaritons. *Rep. Prog. Phys.* **2013**, *76*, 016402.
- Zia, R.; Schuller, J. A.; Chandran, A.; Brongersma, M. L. Plasmonics: The Next Chip-Scale Technology. *Mater. Today* **2006**, *9*, 20–27.
- Ebbesen, T. W.; Genet, C.; Bozhevolnyi, S. I. Surface-Plasmon Circuitry. *Phys. Today* **2008**, *61*, 44–50.
- Pyayt, A. L.; Wiley, B.; Xia, Y.; Chen, A.; Dalton, L. Integration of Photonic and Silver Nanowire Plasmonic Waveguides. *Nat. Nanotechnol.* **2008**, *3*, 660–665.
- Zhang, S.; Xu, H. Optimizing Substrate-Mediated Plasmon Coupling toward High-Performance Plasmonic Nanowire Waveguides. *ACS Nano* **2012**, *6*, 8128–8135.
- Davies, M.; Wochnik, A.; Feil, F.; Jung, C.; Bräuchle, C.; Scheu, C.; Michaelis, J. Synchronous Emission from Nanometric Silver Particles through Plasmonic Coupling on Silver Nanowires. *ACS Nano* **2012**, *6*, 6049–6057.
- Fang, Y.; Li, Z.; Huang, Y.; Zhang, S.; Nordlander, P.; Halas, N. J.; Xu, H. Branched Silver Nanowires as Controllable Plasmon Routers. *Nano Lett.* **2010**, *10*, 1950–1954.
- Wei, H.; Li, Z.; Tian, X.; Wang, Z.; Cong, F.; Liu, N.; Zhang, S.; Nordlander, P.; Halas, N. J.; Xu, H. Quantum Dot-Based Local Field Imaging Reveals Plasmon-Based Interferometric Logic in Silver Nanowire Networks. *Nano Lett.* **2011**, *11*, 471–475.
- Wei, H.; Wang, Z.; Tian, X.; Käll, M.; Xu, H. Cascaded Logic Gates in Nanophotonic Plasmon Networks. *Nat. Commun.* **2011**, *2*, 387.
- Dickson, R. M.; Lyon, L. A. Unidirectional Plasmon Propagation in Metallic Nanowires. *J. Phys. Chem. B* **2000**, *104*, 6095–6098.
- Ditlbacher, H.; Hohenau, A.; Wagner, D.; Kreibig, U.; Rogers, M.; Hofer, F.; Aussenegg, F. R.; Krenn, J. R. Silver Nanowires as Surface Plasmon Resonators. *Phys. Rev. Lett.* **2005**, *95*, 257403.
- Falk, A. L.; Koppens, F. H. L.; Yu, C. L.; Kang, K.; Snapp, N. d.-L.; Akimov, A. V.; Jo, M.-H.; Lukin, M. D.; Park, H. Near-Field Electrical Detection of Optical Plasmons and Single-Plasmon Sources. *Nat. Phys.* **2009**, *5*, 475–479.
- Laroche, T.; Girard, C. Near-Field Optical Properties of Single Plasmonic Nanowires. *Appl. Phys. Lett.* **2006**, *89*, 233119.
- Akimov, A. V.; Mukherjee, A.; Yu, C. L.; Chang, D. E.; Zibrov, A. S.; Hemmer, P. R.; Park, H.; Lukin, M. D. Generation of Single Optical Plasmons in Metallic Nanowires Coupled to Quantum Dots. *Nature* **2007**, *450*, 402–406.
- Gruber, C.; Trügler, A.; Hohenau, A.; Hohenester, U.; Krenn, J. R. Spectral Modifications and Polarization Dependent Coupling in Tailored Assemblies of Quantum Dots and Plasmonic Nanowires. *Nano Lett.* **2013**, *13*, 1–6.
- Schuller, J. A.; Barnard, E. S.; Cai, W.; Jun, Y. C.; White, J. S.; Brongersma, M. L. Plasmonics for Extreme Light Concentration and Manipulation. *Nat. Mater.* **2010**, *9*, 193–204.
- Zhang, D. G.; Yuan, X.-C.; Bouhelier, A.; Wang, P.; Ming, H. Excitation of Surface Plasmon Polaritons Guided Mode by Rhoadmine B Molecules Doped in a PMMA Stripe. *Opt. Lett.* **2010**, *35*, 408–410.
- Drezet, A.; Hohenau, A.; Koller, D.; Stepanov, A.; Ditlbacher, H.; Steinberger, B.; Aussenegg, F. R.; Leitner, A.; Krenn, J. R. Leakage Radiation Microscopy of Surface Plasmon Polaritons. *Mater. Sci. Eng., B* **2008**, *149*, 220–229.
- Massenot, S.; Grandidier, J.; Bouhelier, A.; Colas des Francs, G.; Markey, L.; Weeber, J.-C.; Dereux, A.; Renger, J.; González, M. U.; Quidant, R. Polymer-Metal Waveguides Characterization by Fourier Plane Leakage Radiation Microscopy. *Appl. Phys. Lett.* **2007**, *91*, 243102.
- Hecht, B.; Bielefeld, H.; Novotny, L.; Inouye, Y.; Pohl, D. W. Local Excitation, Scattering and Interference of Surface Plasmons. *Phys. Rev. Lett.* **1996**, *77*, 1889–1892.
- Shegai, T.; Miljković, V. D.; Bao, K.; Xu, H.; Nordlander, P.; Johansson, P.; Käll, M. Unidirectional Broadband Light Emission from Supported Plasmonic Nanowires. *Nano Lett.* **2011**, *11*, 706–711.
- Hohenau, A.; Krenn, J. R.; Drezet, A.; Mollet, O.; Huant, S.; Genet, C.; Stein, B.; Ebbesen, T. W. Surface Plasmon Leakage Radiation Microscopy at the Diffraction Limit. *Opt. Express* **2011**, *19*, 25749–25762.
- Auzel, F. Upconversion and Anti-Stokes Processes with f and d Ions in Solids. *Chem. Rev.* **2004**, *104*, 139–174.
- Rai, P.; Hartmann, N.; Berthelot, J.; Arocás, J.; Colas des Francs, G.; Hartschuh, A.; Bouhelier, A. Electrical Excitation of Surface Plasmons by an Individual Carbon Nanotube Transistor. *Phys. Rev. Lett.* **2013**, *111*, 026804.
- Bharadwaj, P.; Deutsch, B.; Novotny, L. Optical Antennas. *Adv. Opt. Photonics* **2009**, *1*, 438–483.
- Lieb, M. A.; Zavislán, J. M.; Novotny, L. Single-Molecule Orientations Determined by Direct Emission Pattern Imaging. *J. Opt. Soc. Am. B* **2004**, *21*, 1210–1215.
- Curto, A. G.; Volpe, G.; Taminau, T. H.; Kreuzer, M. P.; Quidant, R.; van Hulst, N. F. Unidirectional Emission of a Quantum Dot Coupled to a Nanoantenna. *Science* **2010**, *329*, 930–933.
- Hartmann, N.; Pireddu, G.; Berthelot, J.; Colas des Francs, G.; Bouhelier, A.; Hartschuh, A. Launching Propagating Surface Plasmon Polaritons by a Single Carbon Nanotube Dipolar Emitter. *Nano Lett.* **2012**, *12*, 177–181.
- Taminau, T. H.; Stefani, F. D.; van Hulst, N. F. Optical Nanorod Antennas Modeled as Cavities for Dipolar Emitters: Evolution of Sub- and Super-radiant Modes. *Nano Lett.* **2011**, *11*, 1020–1024.
- Novotny, L. Effective Wavelength Scaling for Optical Antennas. *Phys. Rev. Lett.* **2007**, *98*, 266802.
- Kolesov, R.; Grotz, B.; Balasubramanian, R. J.; Stör, G.; Nicolet, A. A. L.; Hemmer, P. R.; Jelezko, F.; Wrachtrup, J. Wave-Particle Duality of Single Surface Plasmon Polaritons. *Nat. Phys.* **2009**, *5*, 470–474.
- Dorfmüller, J.; Vogelgesang, R.; Khunsin, W.; Rockstuhl, C.; Etrich, C.; Kern, K. Plasmonic Nanowire Antennas: Experiment, Simulation, and Theory. *Nano Lett.* **2010**, *10*, 3596–3603.
- Encina, E. R.; Coronado, E. A. Plasmonic Nanoantennas: Angular Scattering Properties of Multipole Resonances in Noble Metal Nanorods. *J. Phys. Chem. C* **2008**, *112*, 9586–9594.
- Li, Z.; Hao, F.; Huang, Y.; Fang, Y.; Nordlander, P.; Xu, H. Directional Light Emission from Propagating Surface Plasmons of Silver Nanowires. *Nano Lett.* **2009**, *9*, 4383–4386.
- Li, Q.; Qiu, M. Plasmonic Wave Propagation in Silver Nanowires: Guiding Modes or Not? *Opt. Express* **2013**, *21*, 8587.
- Olejnik, M.; Krajnik, B.; Kowalska, D.; Twardowska, M.; Czechowski, N.; Hofmann, E.; Mackowski, S. Imaging of Fluorescence Enhancement in Photosynthetic Complexes Coupled to Silver Nanowires. *Appl. Phys. Lett.* **2013**, *102*, 083703.
- Kumar, R.; Nyk, M.; Ohulchansky, T. Y.; Flask, C. A.; Prasad, P. N. Combined Optical and MR Bioimaging Using Rare Earth Ion Doped NaYF₄ Nanocrystals. *Adv. Funct. Mater.* **2009**, *19*, 853–859.